Soil Dynamics and Earthquake Engineering 141 (2021) 106465

Contents lists available at ScienceDirect

Soil Dynamics and Earthquake Engineering

journal homepage: http://www.elsevier.com/locate/soildyn

Effect of prior small to moderate seismic events on monotonic undrained shear strength of sand

Ting-Wei Wu [a,*], Yusuke Suzuki [b], Brian Carlton [b], Carl Harbitz [b], Achim Kopf [a]

[a] Center for Marine Environmental Sciences (MARUM), University of Bremen, 28359, Bremen, Germany
[b] Norwegian Geotechnical Institute (NGI), N-0855, Oslo, Norway

ARTICLE INFO

Keywords:
Undrained triaxial test
Ottawa sand
Earthquake
Liquefaction
Reconsolidation
Undrained shear strength
Seismic strengthening

ABSTRACT

In this study we investigate the effect of prior seismic shaking on the monotonic shear strength of saturated Ottawa Sand 20/30. We perform a series of stress-controlled undrained cyclic triaxial tests with different seismic intensities intentionally without causing failure, followed by drainage of the excess pore pressure and an undrained monotonic loading test to determine the undrained shear strength. The experimental data show that small to moderate seismic events that do not fail the specimen can significantly increase undrained shear strength without much change in relative density. One prior seismic event with peak ground acceleration ~ 1.3 m/s^2 may increase the undrained shear strength of a specimen at ~ 10 m depth by around 30%. The results also show that as the intensity of the shaking increases, the increase in the monotonic shear strength increases. However, the strengthening effect does not increase with the number of seismic events although a small degree of global densification in the sample is observed. The results of this paper will help assess the change in static slope stability after a single or multiple small to moderate events occurred without causing initial instability.

1. Introduction

Submarine landslides are a major threat to offshore infrastructure and coastal communities because of their large displacements and potential to trigger tsunamis. On active continental margins there are surprisingly fewer observed landslides than passive margins, despite the increase in earthquake activity (e.g. Shanmugan [1]). In addition, Nelson et al. [2] found shorter run-out distances of mass transport deposits on active margins compared with passive margins. Sawyer and DeVore [3] showed from worldwide vane-shear data tested on previously unfailed sediments that active margin sites have consistently higher shear strengths than passive margins by a factor of approximately 2–3, at least until 10 m below the seafloor. It has been proposed that repeated small to moderate earthquakes that do not fail the soil densify it, which leads to higher shear resistance and requires a larger earthquake as a trigger [2,4–6]. This phenomenon is called "seismic strengthening".

Several researchers have investigated the effect of seismic strengthening on liquefaction resistance of cohesionless soils. Wichtmann et al. [7] conducted drained preloading tests on sand to represent minor shaking followed by undrained cyclic loading to determine the increase in its liquefaction resistance. The drained cyclic preloading reduced the rate of pore pressure accumulation in the undrained cyclic loading phase afterwards. Therefore, the sample required more cycles to reach liquefaction after pre-straining. However, during earthquakes there is usually not enough time for pore pressure to dissipate, and it is more reasonable to conduct undrained tests to simulate earthquakes. Teparaska and Koseki [8] conducted a series of repeated liquefaction tests on silica sand #7 with stress-controlled undrained triaxial loading followed by drainage after liquefaction took place. They showed that a sample that already liquefied had the potential to liquefy again, but the potential gradually decreased because of the densification resulting from the drainage (reconsolidation) phases. Wahyudi et al. [9] and Koseki et al. [10] studied re-liquefaction with cyclic stacked ring simple shear tests on Toyoura sand with constant volume followed by reconsolidation. They suggested that the re-liquefaction resistance increases if the double-amplitude shear strain caused by the immediate past liquefaction history was < 5%; otherwise, the re-liquefaction resistance would decrease if the past strain history was too large. Song et al. [11] collected natural submarine silts from non-liquefied and post-liquefied seabed (induced by wave action) in the Yellow River subaqueous delta. Triaxial tests indicated that due to reconsolidation, the monotonic and cyclic

* Corresponding author.
E-mail addresses: tingweiwu@marum.de, tingwei.wu2@gmail.com (T.-W. Wu).

https://doi.org/10.1016/j.soildyn.2020.106465
Received 6 January 2020; Received in revised form 14 July 2020; Accepted 6 October 2020
Available online 6 December 2020

strengths in the post-liquefied area were both increased in comparison to non-liquefied soil.

Most seismic strengthening studies so far have only examined the change in a sample's dynamic resistance by cyclic loading (e.g. re-liquefaction potential), but little is known about the change in its static resistance by monotonic loading (e.g. undrained shear strength, the resistance to trigger a landslide without dynamic sources like earthquakes or wave actions). In addition, it remains unknown how sediment composition affects seismic strengthening and whether there is a maximum strength that can be achieved after multiple events. Therefore, additional research related to seismic strengthening is necessary.

In this study, 16 cyclic and monotonic triaxial tests were performed on Ottawa Sand 20/30 to investigate the effects of cyclic loading and reconsolidation on post-cyclic monotonic loading. We first perform stress-controlled, undrained cyclic triaxial tests on the specimens without causing them to fail. We then dissipate the excess pore pressure by allowing drainage and conduct undrained monotonic tests to determine the undrained shear strength. The objective of this study is to estimate the change in the monotonic undrained shear strength due to prior cyclic loading. This is extremely important to assess the change in the static slope stability after a single or multiple earthquakes that do not cause failure.

2. Simplified procedure for estimating stresses induced by an earthquake

For experimental liquefaction analyses, Seed and Idriss [12] and Idriss [13] developed a simplified procedure to convert an earthquake acceleration time series into an equivalent number of uniform loading cycles (N_{eq}) at a given equivalent cyclic shear stress ratio (CSR_{eq}) for a specific depth z (m):

$$CSR_{eq} = 0.65 \times \frac{\sigma_v}{\sigma'_v} \times \frac{a_{max}}{g} \times r_d \quad (1)$$

where σ_v is the total vertical stress (Pa) at depth z, σ'_v is the effective vertical stress (Pa) at depth z, a_{max} is the maximum ground surface acceleration in m/s^2 (also called PGA, peak ground acceleration), g is gravitational acceleration (~9.81 m/s^2), and r_d is a stress reduction factor expressed as in Youd et al. [14]:

$$r_d = \frac{(1.000 - 0.4113z^{0.5} + 0.04052z + 0.001753z^{1.5})}{(1.000 - 0.4177z^{0.5} + 0.05729z - 0.006205z^{1.5} + 0.001210z^2)} \quad (2)$$

in which z is the sample's depth in meters. These equations were formed empirically with $N_{eq} = 15$ and past earthquake data with magnitudes of approximately 7.5. For other magnitudes than 7.5, Idriss [13] and Youd et al. [14] provide tables to adjust N_{eq}, and magnitude scaling factors to adjust eq.(1). In this work, we perform 15 cycles in a traixial device (i.e. $N_{eq} = 15$) corresponding to magnitude 7.5 earthquakes, but with different CSR_{eq} to simulate different "seismic intensities" (a_{max}). Note that the above equations are only applicable on samples at depths < 20 m because liquefaction evaluations at greater depths require more detailed site response analyses with sufficient subsurface characterization [15].

3. Grain size analysis and maximum and minimum void ratio determination of Ottawa Sand 20/30

We use Ottawa Sand 20/30, a sand mined from the Ottawa, Illinois area in the USA used in some previous liquefaction studies (e.g. Polito et al. [16]). Ottawa Sand 20/30 is a rounded, poorly-graded coarse sand. According to the certificate of analysis from the producer [17], 100% of the mineralogy is quartz, and its specific gravity (Gs) is 2.635–2.66 at 20 °C. In this study, we use Gs = 2.65.

Fig. 1 shows the grain size distribution curve. The median particle size (D_{50}) is approximately 0.73 mm, and the coefficient of uniformity ($Cu = D_{60}/D_{10}$) is about 1.22. The minimum void ratio (e_{min}) was determined by vibrating thin layers of sand in a mold for 30 s each. The maximum void ratio (e_{max}) was determined by retracting a tube that allows sand to fall inside a mold below and averaging the density values obtained from 5 tests. More details of the method are described in Refs. [18] (NGI dry method). These values are used to calculate the relative density (D_R), which is defined as:

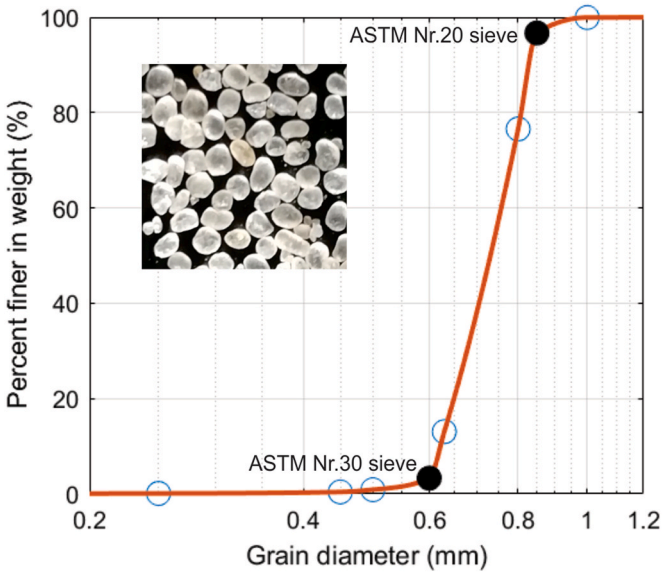

Fig. 1. Photograph of Ottawa Sand 20/30 and grain size distribution curve obtained with two ASTM sieves [17] marked as black dots and six additional sieves marked as blue circles. The red curve is calculated with shape-preserving piecewise cubic interpolation. (For interpretation of the references to colour in this figure legend, the reader is referred to the Web version of this article.)

$$D_R = \frac{e_{max} - e}{e_{max} - e_{min}} \times 100\% \quad (3)$$

where e is the void ratio of the prepared sample for further testing.

Table 1 shows the comparison of the determined e_{max} and e_{min} with three other papers. Table 1 shows that our values are similar to Polito et al. [16]; but smaller than the other two studies. This has a significant effect on the calculated relative density for a given void ratio. An example of void ratio 0.65 used in the experiments in Polito et al. [16] results in D_R ranging between 21% and 46% by different e_{max} and e_{min} determinations. Thus, comparison of sand densities in different papers should be based on void ratios, or by D_R calculated with the same e_{min} and e_{max} values.

4. Triaxial sample preparation

Triaxial tests are performed at the Norwegian Geotechnical Institute (NGI) using an Advanced Dynamic Triaxial Testing System (DYNTTS)

Table 1
Comparison of determined maximum and minimum void ratios (e_{max}, e_{min}) of Ottawa Sand 20/30 in different studies.

	e_{min}	e_{max}	Calculated D_R with e = 0.65
[31]	0.502	0.742	38%
[50]	0.50 (alternative method)	0.78 (ASTM D4254)	46%
[16]	0.46	0.70	21%
This study	0.469 (NGI dry method)	0.711 (NGI dry method)	25%

with up to 5 Hz and 10 kN capabilities manufactured by the GDS instruments Ltd [19]. The cell is screw-driven from an integral base unit housing the motor drive, which allows the axial load to be applied through the base of the cell. The axial load is measured by a load cell placed on top of the specimen. The triaxial cell top is removable to allow the test specimen to be prepared in place. NGI in-house bender elements [20] are mounted in the triaxial system, which allow the calculation of the specimen's small strain shear modulus (Gmax) with shear wave velocity measurement (Appendix A; Appendix B).

Moist-tamped specimens are prepared by placing predetermined quantities of soil in a mold in six layers and carefully compacting each layer to the desired density using a flat-bottom tamper and supporting equipment developed by NGI that allows an accurate height control of each layer. NGI also developed a modified under-compaction method after Ladd [21] with initial water content chosen to be 3% in this study. The first (bottom) layer is compacted to slightly lower density than succeeding layers with under-compaction factor of 0.03 (definition in Ref. [21]). The interface of each succeeding layer is crisscrossed with a spatula to avoid distinct layering. After placing a top cap on the sixth layer, a suction of about 20 kPa is applied, and the height and circumference of the specimen are measured to calculate the specimen's dimension. Target values are 5.4 cm in diameter and 10.8 cm in height, with a sand mass of around 397 g to form $D_R \sim 21\%$ before consolidation.

After mounting, the sample is flushed with CO_2 for 20 min, saturated with de-aerated water under a cell pressure of 20 kPa, and a back-pressure of around 500 kPa is applied with a rate of 0.2 kPa/s to obtain better saturation in the specimen. Saturation is checked by decreasing and increasing the confining stress by 30 kPa to obtain a minimum Skempton's B-value of 0.96 [22]. After saturation, all specimens are isotropically-consolidated to a mean effective stress of 100 kPa with a rate of 0.1 kPa/s. Consolidation is typically kept for 2 h, and is considered finished when axial displacement change is ≤ 0.001 mm and volume change is $\leq 2\ mm^3$ within 5 min. Mean effective stress is defined by:

$$p' = \frac{\sigma_1 + 2\ \sigma_3}{3} - u \tag{4}$$

where σ_1 is the major principal stress (in the axial direction), σ_3 is the minor principal stress (in the radial direction), and u is the pore pressure. Deviator stress q is the difference between principal stresses, which is defined by:

$$q = \sigma_1 - \sigma_3 \tag{5}$$

The sample undergoes densification during consolidation; therefore, final relative density is recalculated by the volume change of the specimen and is close to 25%. Maximum shear modulus (Gmax) is subsequently measured with bender elements (Appendix B).

5. Monotonic and cyclic triaxial testing procedures

We perform monotonic and cyclic experiments with a similar state after consolidation (void ratio $e \sim 0.65$, relative density $D_R \sim 25\%$ and mean effective stress $p' \sim 100$ kPa) but with different cyclic shear stress ratios (CSR) to investigate the influence of an earthquake's intensity on seismic strengthening. In all of the tests, we correct the deviator stresses for the membrane and we compute the cross-sectional areas based on a simplified assumption that the specimens deform as right circular cylinders during shear [23].

5.1. Undrained monotonic loading

We conduct monotonic shear tests by compressing the sample in the vertical (axial) direction with 0.1 mm/min while keeping the lateral (radial) stress constant. Wang and Luna [24] compared several failure criteria of silt, and suggested "limiting strain" to be the best one owing to better consistency and rational results of the friction angle. In this study, undrained shear strength (τ_{max5}) is defined by:

$$\tau_{max5} = \frac{q_5}{2} \tag{6}$$

where q_5 is the maximum deviator stress before or at the time when 5% axial strain (ε_a) is achieved. The 5% conventional axial strain limit is made to be consistent with the strain failure criterion of cyclic loading in the following section.

5.2. Undrained cyclic loading

We perform cyclic shear tests with harmonic stress-controlled compression – extension in the axial direction. Most tests are conducted at a frequency of 1 Hz, which is a standard frequency used in earthquake engineering [25], and a few tests are conducted with 0.5 Hz. For sands, the cyclic frequency of the wave loading has negligible effect on the cyclic strength, as shown by data from other laboratory studies (e.g. Ref. [26–28]). The radial stress is kept constant. The GDS device has an adaptive control function to estimate the soil's stiffness change during the process of cyclic loading to maintain the target load [29]. The cyclic shear stress ratio (CSR) is calculated by normalizing the cyclic shear stress τ_{cyc} (one-way amplitude of the imposed maximum cyclic shear stress, which is half of the value of the cyclic deviator stress q_{cyc}) over the effective confining stress at the end of consolidation (σ'_{3c}):

$$CSR = \frac{\tau_{cyc}}{\sigma'_{3c}} = \frac{q_{cyc}}{2\ \sigma'_{3c}} \tag{7}$$

We calculate an average CSR from the first loading cycle until the cycle of failure. The excess pore pressure ratio (r_u) is calculated throughout the process, which is the measured excess pore pressure (Δu) normalized to σ'_{3c}:

$$r_u = \frac{\Delta u}{\sigma'_{3c}} \tag{8}$$

In a cyclic test, a sample is considered failed when 5% double-amplitude axial strain is reached [30] (termed "strain failure") and/or when the excess pore pressure ratio exceeds 0.95 (termed "liquefaction"). The first failure criterion represents softening of the soil, and the second represents when there is enough pore pressure buildup to make the soil reach a state close to zero effective stress. We test samples at different CSR values and obtain the number of cycles to failure (NOC). We then fit a polynomial interpolation curve through the CSR-log(NOC) space to represent the sediment's cyclic shear resistance during earthquakes. We define CSR_{15} as the CSR required for the sample to reach failure in 15 cycles.

5.3. Test series

Fig. 2 shows the testing procedure. First, we perform undrained monotonic and cyclic shear tests on "fresh" reconstituted specimens to obtain their shear resistance (τ_{max5} and CSR_{15}). Next, we prepare another sample with the same initial conditions and impose a smaller earthquake (15 cycles with a CSR smaller than CSR_{15}) to ensure that the sample does not fail. Then, we drain the sample with sufficient time (~1 h) to dissipate the excess pore pressure for reconsolidation. The same as consolidation, drainage is considered finished when axial displacement change is ≤ 0.001 mm and volume change is $\leq 2\ mm^3$ over a 5 min time period. The undrained cyclic loading simulates an earthquake when it happens, and the following drainage simulates the condition in the field when there is sufficient time for the sediment to reconsolidate. The undrained cyclic loading and the following drainage defines one "seismic event". Finally, we conduct an undrained monotonic test and measure the sample's undrained shear strength again (τ_{max5}). In this way, the undrained shear strength after reconsolidation can be

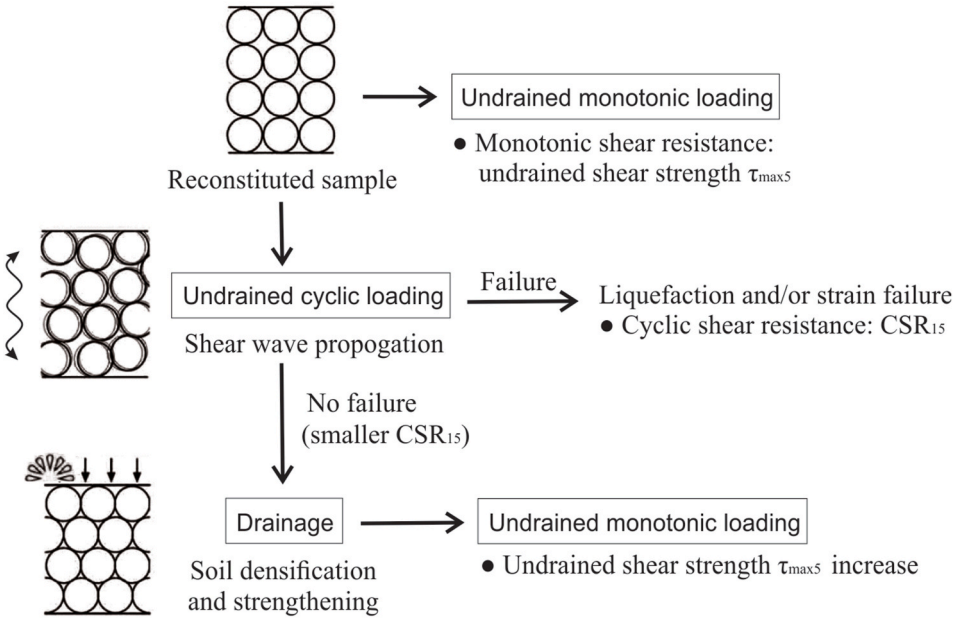

Fig. 2. Schematic diagram for the procedure of monotonic/cyclic and post-cyclic shear tests to assess seismic strengthening. CSR_{15}: cyclic shear stress ratio required to reach failure in 15 cycles; τ_{max5}: maximum shear stress of the sample before or at the time when 5% axial strain is achieved.

compared to the strength of a fresh sample.

6. Triaxial testing results

Table 2 presents a summary of test results. All tests are consolidated to a target confining pressure of 100 kPa, whereas actual values range from 98.8 kPa to 102.0 kPa.

6.1. Stress-strain behavior and shear strength parameters from monotonic loading tests

Fig. 3 compares the monotonic testing results on loose samples ($D_R \sim 25\%$, saturated density around 2000 kg/m^3) and a very loose sample ($D_R \sim 7\%$, saturated density around 1974 kg/m^3) of Ottawa Sand 20/30. In Fig. 3ef, Test26 shown as blue and Test9 shown as yellow are two tests intended to be done with the same condition ($D_R \sim 25\%$). The two tests demonstrate very good repetition of the stress-strain patterns, showing that the sand reconstitution method used in this study is capable of reproducing specimens. Fig. 3ae and Fig. 3bf show the patterns of deviator stress and excess pore pressure ratio with axial strain. The very loose sample ($D_R \sim 7\%$) demonstrates limited strain softening behavior with a peak deviator stress observed at $\varepsilon_a \sim 0.6\%$. The $D_R \sim 25\%$ samples demonstrate slightly increasing pore pressure with strain before decreasing and becoming negative. This decrease is because of a tendency of the soil to dilate. They therefore demonstrate strain hardening behavior with increasing deviator stress. The difference of strain softening (contractive) and strain hardening (dilative) behaviors is due to the different void ratio positions relative to the critical void ratio line, consistent with the undrained triaxial test results by Santamarina and Cho [31] (Appendix C).

Calculation of shear modulus degradation during shear is explained in Appendix D. We normalize the shear modulus by Gmax obtained from bender element tests after consolidation, and obtain a non-linear curve of G/Gmax versus shear strain (Fig. 3cg). The shear modulus degrades quickly within the range of 1% shear strain in both cases, but the initial shear modulus of the $D_R \sim 7\%$ sample (89.6 MPa) is smaller than the $D_R \sim 25\%$ sample (100.6 MPa), see also Table 2.

Fig. 3dh represents the approximate Mohr-Coulomb envelop at failure (5% axial strain limit as defined in eq.(6)). Definitions of the coordinates are:

$$\sigma' = \frac{\sigma_1 + \sigma_3}{2} - u \tag{9}$$

$$\tau = \frac{\sigma_1 - \sigma_3}{2} \tag{10}$$

Undrained shear strength (τ_{max5}) of a $D_R \sim 7\%$ specimen is 41 kPa when the shear stress reaches a peak at $\varepsilon_a \sim 0.6\%$ before the strain limit 5% is achieved, and a $D_R \sim 25\%$ specimen is 170 kPa picked at $\varepsilon_a = 5\%$.

The angle of shearing resistance (also called friction angle) using 5% axial strain limit (ϕ'_5) is calculated with a tangent line intersecting the Mohr-circle assuming zero cohesion intercept on the shear stress axis (i.e. there is no cementation or other bonding between the particles). It is around 22° for the very loose sample ($D_R \sim 7\%$) and 28° for the loose sample ($D_R \sim 25\%$). The value 28° is consistent with the friction angle determined by Santamarina and Cho [31] for their critical state undrained test results on Ottawa Sand 20/30. Comparing with other friction angles determined by Santamarina and Cho [31] (from 30° of "ASTM graded sand" to 34° of "Blasting sand"), Ottawa Sand 20/30 demonstrates a relatively lower frictional property than the other kinds of sand.

In the study by Denekamp and Tsur-Lavie [32]; it was shown that very loose sediment rarely exists in natural environments, and can only be found in slip deposits formed by avalanching. In this study, we only aim to test the level ground condition; therefore, we only choose $D_R \sim 25\%$ to test seismic strengthening hereafter. However, it is evident from the above-mentioned comparison of undrained shear strength, shear modulus, and friction angle on $D_R \sim 7\%$ and $D_R \sim 25\%$ specimens that initial density is an important parameter that controls the initial shear strength properties of a reconstituted specimen.

6.2. Liquefaction and strain failure from cyclic loading tests

Fig. 4 shows the response of Test20 with $D_R \sim 25\%$ and CSR = 0.189 subjected to cyclic loading. The figure presents the applied deviator stress (Fig. 4a), the axial strain (Fig. 4b), and the excess pore pressure ratio (Fig. 4c) versus the number of cycles, as well as the stress path in the p'-q space (Fig. 4d). Fig. 4c shows that r_u accumulates incrementally to 50% until a sudden increase takes place to almost 100%, causing the soil to reach a state of nearly zero effective stress. Fig. 4b shows that the

Table 2
Summary of initial conditions and the testing results. All tests are consolidated to p'~ 100 kPa.

	Initial state after reconstitution		State after consolidation				Cyclic loading1			State after drainage1		Cyclic loading2			State after drainage2		Monotonic undrained shear strength with 5% axial strain limit τ_{max5} (kPa)	Effective friction angle with 5% axial strain limit ϕ'_5 (°)
Lab ID	Void ratio e_i	Relative density D_{Ri} (%)	Void ratio e_c	Relative density D_{Rc} (%)	B value	Small strain shear modulus $Gmax_c$ (MPa)	Cyclic shear stress ratio CSR1	Number of cycles NOC1 [strain failure/ liquefaction[a]]	Pore pressure increase Δu1 (kPa)	Relative density D_{Rd1} (%)	Small strain shear modulus $Gmax_{d1}$ (MPa)	Cyclic shear stress ratio CSR2	Number of cycles NOC2	Pore pressure increase Δu2 (kPa)	Relative density D_{Rd2} (%)	Small strain shear modulus $Gmax_{d2}$ (MPa)		
Test8	0.669	17.4	0.659	21.7	0.96	[b]	0.194[c]	[20/20] (failure)	> 95.0									
Test16	0.660	21.3	0.648	26.1	1.00	96.9	0.200[c]	[4/4] (failure)	> 95.0									
Test18	0.663	19.8	0.653	23.9	1.00	91.9	0.188[c]	[9/9] (failure)	> 95.0									
Test19	0.655	23.0	0.645	27.1	1.00	97.6	0.178[c]	[982/983] (failure)	> 95.0									
Test20	0.663	20.0	0.652	24.2	0.99	97.5	0.189[d]	[13/13] (failure)	> 95.0									
Test31	0.658	21.9	0.648	26.0	0.98	98.8	0.200[d]	[3/4] (failure)	> 95.0									
Test38	0.707	1.8	0.694	7.2	1.00	89.6					Monotonic						40.7	22.2
Test9	0.666	18.6	0.653	24.0	0.96	[b]					Monotonic						167.8	28.0
Test26	0.660	21.0	0.650	25.1	1.00	100.6					Monotonic						170.2	27.9
Test25	0.656	22.8	0.646	27.0	1.00	95.8	0.146[c]	15 (no failure)	9.1	27.3	97.9			Monotonic			199.6	28.2
Test21	0.654	23.5	0.644	27.8	1.00	95.8	0.143[c]	15 (no failure)	10.0	28.1	97.9	0.150[c]	15 (no failure)	2.1	28.2	97.0	183.6	27.9
Test33[e]	0.658	22.0	0.647	26.3	0.98	101.5	0.147[c]	15 (no failure)	10.7	26.6	100.2	0.148[c]	15 (no failure)	1.9	26.7	100.2	189.6	28.0
Test12	0.657	22.4	0.645	27.3	0.99	[b]	0.165[c]	15 (no failure)	11.8	27.6	[b]			Monotonic			228.6	28.4
Test24	0.655	23.1	0.645	27.5	1.00	96.9	0.161[c]	15 (no failure)	11.6	27.8	99.1	0.166[c]	15 (no failure)	2.8	27.9	98.7	210.1	28.1
Test32[e]	0.654	23.5	0.643	28.1	1.00	96.2	0.168[d]	15 (no failure)	17.9	28.7	97.9	0.170[c]	15 (no failure)	2.7	28.8	97.5	165.4	27.5
Test39	0.654	23.6	0.644	27.7	0.99	102.8	0.147[d]	15 (no failure)	10.6	28.0	102.4	0.167[d]	15 (no failure)	3.8	28.1	101.5	190.2	27.9

[a] Decimals are rounded up to integers.
[b] No measurement.
[c] Frequency 1 Hz.
[d] Frequency 0.5 Hz.
[e] Five cyclic loading events. Cyclic loading and drainage data after the second event are not presented here for the concision.

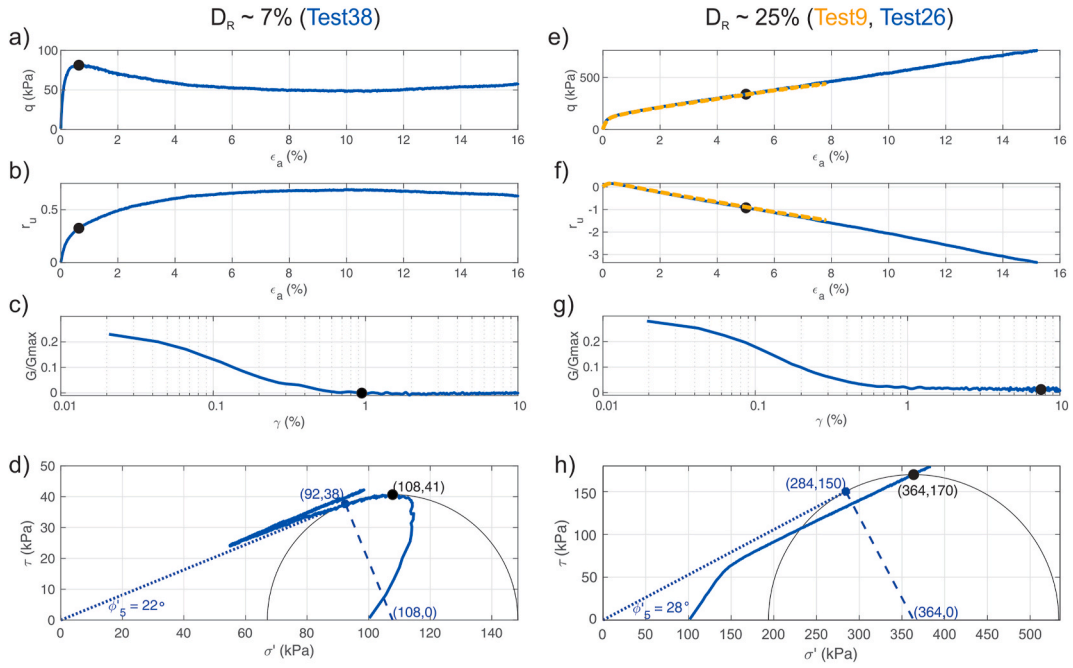

Fig. 3. Undrained monotonic test results conducted at p' ~ 100 kPa. Black dots mark the points where undrained shear strength (maximum shear stress before or at the time of 5% axial strain) is calculated. (abcd) Test38 conducted at D_R ~ 7%. Undrained shear strength is 41 kPa. (efgh) Test26 in blue and its repetition test in yellow (Test9). Both tests are conducted at D_R ~ 25%. Undrained shear strength is 170 kPa. (For interpretation of the references to colour in this figure legend, the reader is referred to the Web version of this article.)

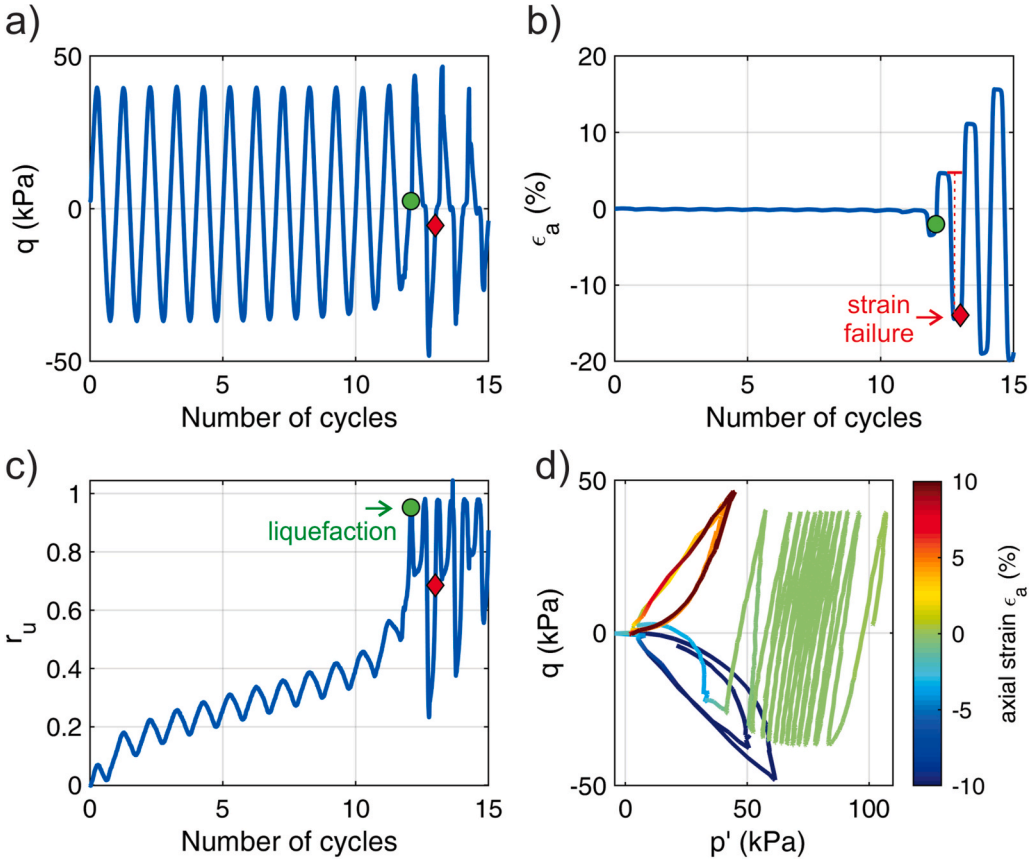

Fig. 4. Results of Test20, tested at D_R ~ 25%, p' ~ 100 kPa, and 0.5 Hz. (a) Deviator stress versus number of cycles. CSR = 0.189. (b) The sample reaches strain failure when double-amplitude axial strain $\varepsilon_{da} \geq 5\%$ at the 13th cycle marked as a red diamond. (c) The sample liquefies at the 13th cycle marked as a green circle (when $r_u \geq 0.95$). (d) p'-q stress path. Color indicates the axial strain. (For interpretation of the references to colour in this figure legend, the reader is referred to the Web version of this article.)

sample deforms very little during the early loading phase, but experiences a sudden increase in axial strain in the extension domain just before liquefaction. After the sample liquefies, large axial deformation is easily triggered without much applied stress. Test results in this study show that strain failure and liquefaction happen mostly at the same time. For example, Test20 had strain failure at the 13th cycle and

liquefaction also at the 13th cycle.

Filled black squares in Fig. 5 show six test results of CSR versus the number of cycles to cause failure. We fit a polynomial interpolation curve through the data to estimate $CSR_{15} = 0.190$ (dashed black curve in Fig. 5). Under effective confining stress of 100 kPa (approximate depth 10.2 m) and according to eq.(1), $CSR_{15} = 0.190$ suggests that the sample will fail when an earthquake happens with peak ground acceleration (a_{max}) larger than 1.59 m/s^2 (0.16 g). We also plot data from Polito et al. [16] with the same void ratio (0.65) and effective stress (100 kPa) in blue for comparison purpose, and for consistency, D_R of these data is recalculated to be 25% using $e_{min} = 0.469$ and $e_{max} = 0.711$ determined by the NGI method used in this study (Table 1). Their data demonstrate higher CSR probably due to the different sample preparation method in their study (dry deposition). Compared with our study, they also had bigger specimen dimension (7.1 cm in diameter and 15.4 cm in height).

6.3. Effects of seismic intensity and number of events on seismic strengthening

In this study we tested two levels of moderate earthquakes in the Japanese JMA Scale [33] and the Taiwanese CWB Scale [34]. When we apply 15 cycles of CSR ~ 0.147, approximate peak ground acceleration (a_{max}) according to eq.(1) is ~ 1.23 m/s^2 (0.13 g), which corresponds to an instrument intensity scale of "5-lower" in the JMA and CWB Scales. When CSR ~ 0.167, a_{max} according to eq.(1) is ~ 1.40 m/s^2 (0.14 g), which corresponds to "5-upper" in the JMA and CWB Scales. This is a simplified approximation of intensity as we do not take into account the duration of shaking in real earthquake cases [35,36]. Since these two levels of seismic intensities (i.e. 15 cycles of different CSRs) are plotted below the cyclic strength curve determined in the previous section, they are not strong enough to cause failure (green stars in Fig. 5).

Fig. 6 demonstrates an example of seismic strengthening test with two levels of prior seismic events (Test39). The sample is first consolidated to D_R ~ 25% and p' ~ 100 kPa. 15 cycles of CSR ~ 0.147 are applied with the drainage valves closed to simulate an earthquake of a_{max} ~ 1.23 m/s^2. The earthquake increases the pore pressure by about 11 kPa (i.e. it makes the mean effective stress p' to drop to about 89 kPa). Subsequently, we open the drainage valves to allow the excess pressure to dissipate. It reconsolidates the sample back to 100 kPa. The second earthquake without failure (15 cycles of CSR ~ 0.167 with a_{max} ~ 1.40 m/s^2) is applied undrained which causes the pore pressure to increase by about 4 kPa. Then, we allow drainage again for reconsolidation. Finally, the sample is tested by monotonic loading until at least 5% axial strain is reached to determine the undrained shear strength after seismic strengthening. Volumetric strain (ε_v) is defined by:

$$\varepsilon_v \sim \frac{-\Delta V}{V} = \frac{-\Delta e}{1+e} \tag{11}$$

where e is the void ratio, and V is the sample volume. In this test, V = 246.99 cm^3 after consolidation. Compressive ε_v is regarded as positive.

Fig. 7 shows the effect of shaking a specimen but not failing it on the subsequent monotonic loading test. For comparison, the residual axial strain after cyclic loading and drainage is resumed back to 0% before the undrained monotonic loading phase (i.e. we substitute the initial sample height with the new height after drainage). The blue curve in Fig. 7a shows that the fresh specimen (Test26, without prior shaking) has τ_{max5} of about 170 kPa. The dashed brown curve shows the result of Test25, which is subjected to one round of shaking (15 cycles of CSR ~ 0.147) and then drainage before the monotonic test. The steeper shear stress increase is caused by the steeper pore pressure decrease (Fig. 7b).

The change of relative density, maximum shear modulus, and undrained shear strength after each drainage stage is listed in Table 3. Although the relative density in Test25 increases by only 1.1%, the increase of undrained shear strength is about 30 kPa (τ_{max5} ~ 200 kPa, an 17.3% increase). The Gmax value after the drainage (reconsolidation) stage also increases from 95.8 MPa to 97.9 MPa (2.2% increase). The steeper slope of Test25 compared with Test26 also means an increase in the sample's Young's modulus (eq. D.1). This is similar to the results of

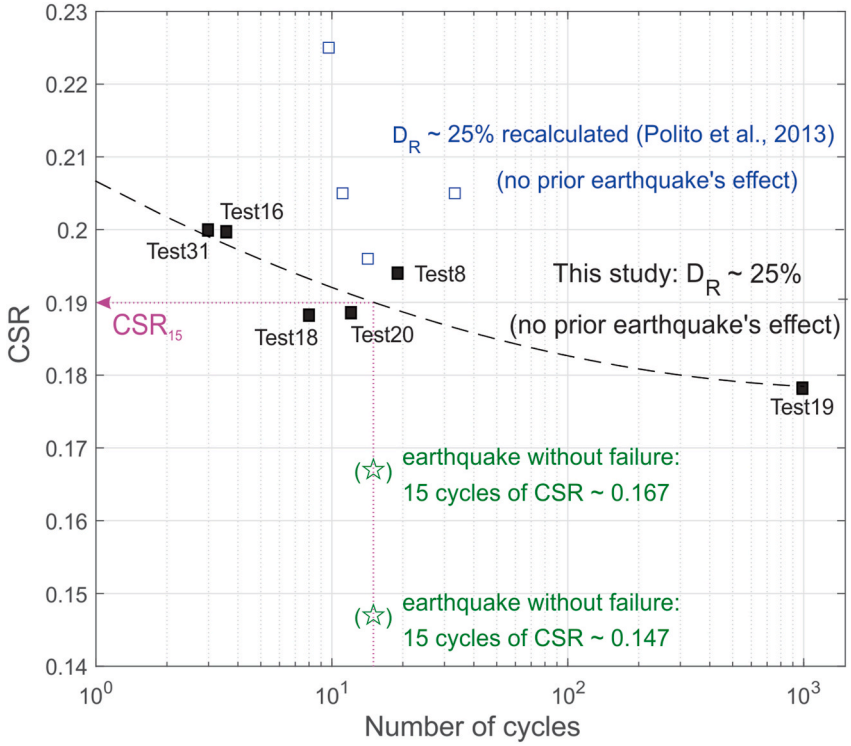

Fig. 5. Cyclic strength curve at D_R ~ 25% and p' ~ 100 kPa obtained with polynomial interpolation of six test results marked as black filled squares. CSR_{15} is 0.190 in this curve. Data points from Polito et al. [16] are plotted for comparison (blue unfilled squares). Two levels of earthquakes without failure tested in this study are shown with green stars. (For interpretation of the references to colour in this figure legend, the reader is referred to the Web version of this article.)

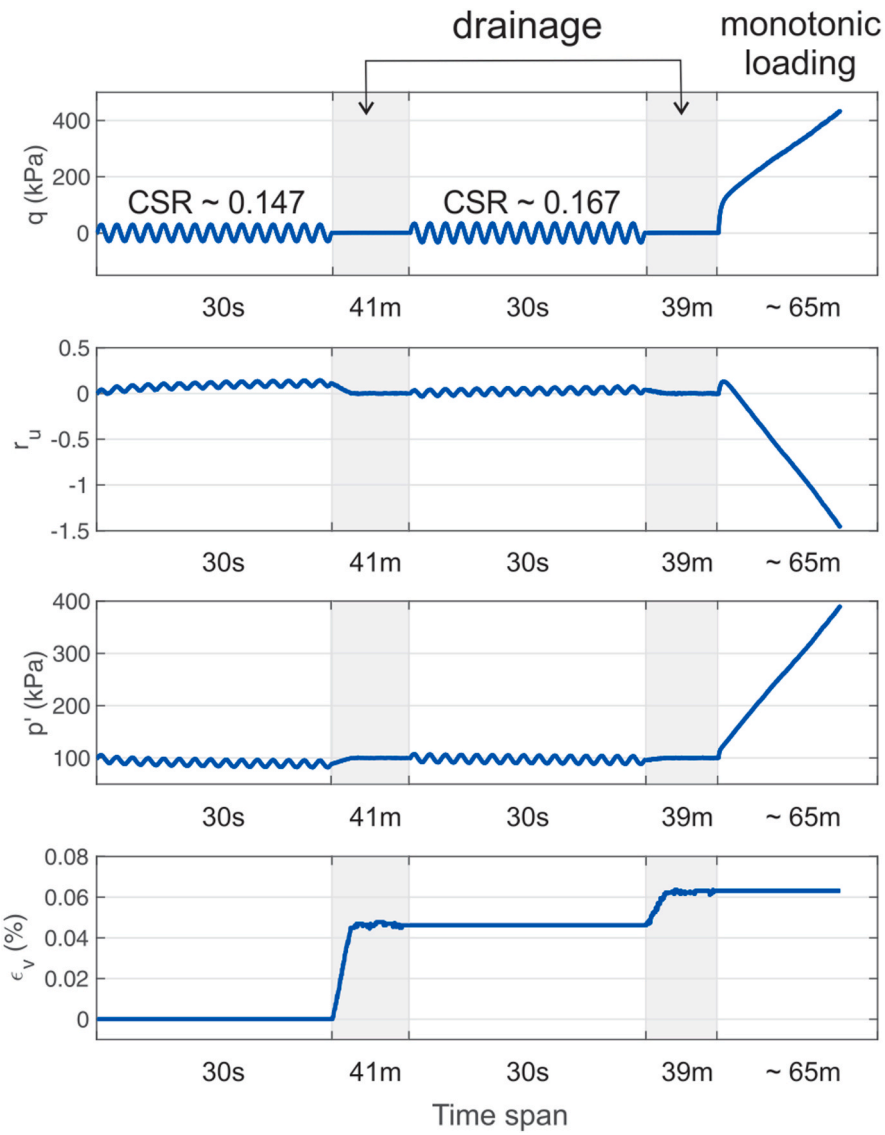

Fig. 6. Time history of Test39, a typical seismic strengthening test for simulating an earthquake without failure (15 cycles of CSR ~ 0.147) followed by drainage, and another earthquake without failure (15 cycles of CSR ~ 0.167) followed by drainage. After the seismic events, the sample goes under monotonic loading until at least 5% axial strain is reached.

Toki and Kitago [37]; who observed an increase in Young's modulus of a loose dry sand that underwent several hundred cycles of small-amplitude vibratory stresses.

However, in the case of two rounds of seismic events (Test21, dashed green curve in Fig. 7a) with similar intensity (15 cycles of CSR ~ 0.147), although relative density still slightly increases after drainage, the undrained shear strength decreases with respect to the case with just one round of seismic event. It is still larger than the fresh specimen. The Gmax value after the second drainage stage ($Gmax_{d2}$, 97.0 MPa) also slightly decreases with respect to the first one ($Gmax_{d1}$, 97.9 MPa). Fig. 7a also shows that a larger CSR that does not fail the specimen results in more strengthening of the sample. In Test12 (dotted brown curve in Fig. 7a), the undrained shear strength increases by 34.3% due to one round of prior seismic event with 15 cycles of CSR ~ 0.167. Similar to the case before, the second seismic event seems to have a destructive effect that decreases the undrained shear strength with respect to the case with just one event (Test24, dotted green curve in Fig. 7a).

Fig. 8a demonstrates the evolution of the undrained shear strength with up to five seismic events. The smaller (CSR ~ 0.147) events demonstrate a somewhat stabilized undrained shear strength after five events (Test33), whereas five bigger (CSR ~ 0.167) events (Test32) demonstrate a decrease of undrained shear strength to even lower than that without any seismic events (Test26). Test39 that undergoes a smaller seismic event and then a bigger seismic event has an undrained shear strength value between the previous two curves. The details of Test32 (five events of 15 cycles of CSR ~ 0.167) are shown in Fig. 8b. Pore pressure becomes less likely to increase after multiple seismic events (unfilled blue circles). Relative density after each drainage stage keeps increasing but with incrementally smaller steps, showing a stabilizing trend. Gmax measurements are made directly after each cyclic loading phase (unfilled orange diamonds), and after each drainage phase (filled orange diamonds). Immediately after each undrained cyclic loading, Gmax decreases due to the decrease in effective stress, but increases after reconsolidation. In Test32, Gmax after reconsolidation increases after the first seismic event, but starts to decrease from the second event onwards. The Gmax after the fifth drainage stage drops to a smaller value than the Gmax before the first cyclic loading phase, showing a similar trend like the undrained shear strength's evolution of CSR ~ 0.167 events presented in Fig. 8a (dotted blue curve). In Test32, the undrained cyclic loading phases induce only small axial strain

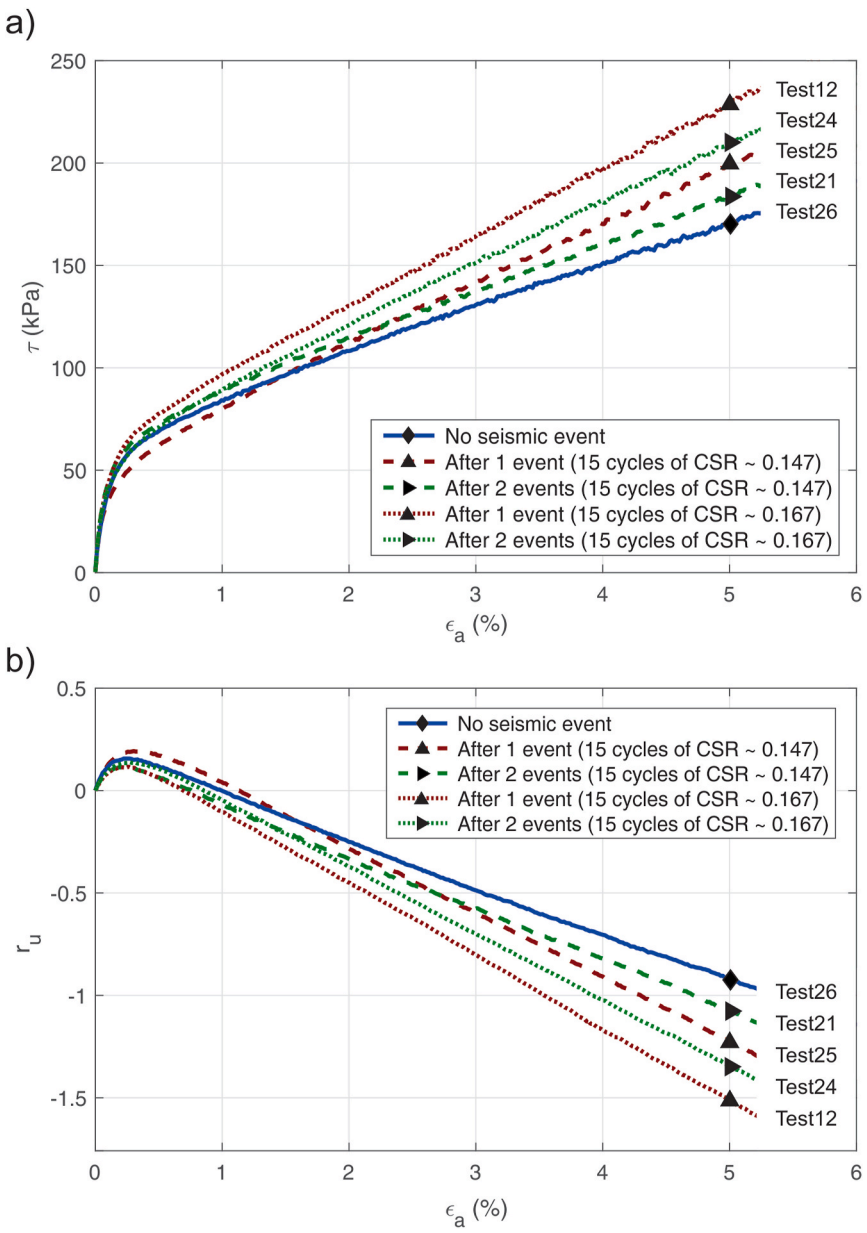

Fig. 7. Monotonic seismic strengthening testing results conducted at p' ~ 100 kPa and D_R ~ 25%. One or two events with different seismic intensities (15 cycles of CSR ~ 0.147 or CSR ~ 0.167) are tested. Blue curves are Test26 without strengthening. (a) Shear stress versus axial strain. Black markers mark the points where the undrained shear strengths τ_{max5} are determined. (b) Pore pressure ratio versus axial strain. (For interpretation of the references to colour in this figure legend, the reader is referred to the Web version of this article.)

Table 3
Change of D_R, Gmax and τ_{max5} after each seismic event (earthquake followed by drainage). We take $\tau_{max5c} = 170.2$ kPa as the undrained shear strength without prior shaking (result of Test26 in Table 2).

"Earthquake"	Lab ID	After one seismic event			After two seismic events			After five seismic events		
		$(D_{Rd1}-D_{Rc})/D_{Rc}$	$(Gmax_{d1}-Gmax_c)/Gmax_c$	$(\tau_{max5}-\tau_{max5c})/\tau_{max5c}$	$(D_{Rd2}-D_{Rc})/D_{Rc}$	$(Gmax_{d2}-Gmax_c)/Gmax_c$	$(\tau_{max5}-\tau_{max5c})/\tau_{max5c}$	$(D_{Rd5}-D_{Rc})/D_{Rc}$	$(Gmax_{d5}-Gmax_c)/Gmax_c$	$(\tau_{max5}-\tau_{max5c})/\tau_{max5c}$
15 cycles of CSR ~ 0.147	Test25	1.1%	2.2%	17.3%						
	Test21	1.1%	2.2%	?	1.4%	1.3%	7.9%			
	Test33	1.1%	-1.3%	?	1.5%	-1.3%	?	1.5%	-2.2%	11.4%
15 cycles of CSR ~ 0.167	Test12	1.1%	?	34.3%						
	Test24	1.1%	2.3%	?	1.5%	1.9%	23.4%			
	Test32	2.1%	1.8%	?	2.5%	1.4%	?	2.8%	-0.4%	-2.8%

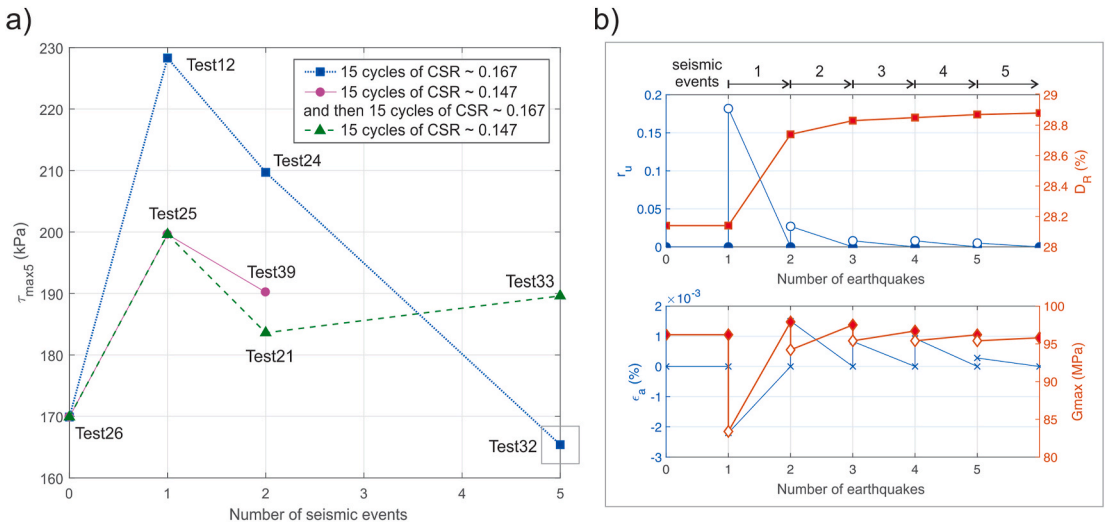

Fig. 8. (a) Evolution of the undrained shear strength of $D_R \sim 25\%$ specimens with different seismic intensity and number of seismic events. (b) Details of Test32 showing the evolution of a $D_R \sim 25\%$ specimen under 5 events of 15 cycles of CSR ~ 0.167. Unfilled markers of r_u and Gmax indicate the measurements made immediately after the cyclic loading phases, and filled markers indicate the measurements after (re)consolidation.

values, but it is worth noticing that the axial strain change is negative in the first cyclic loading phase, and positive in the following cyclic loading phases.

7. Discussion

7.1. Significant change in undrained shear strength due to prior seismic event without significant change in relative density

From Fig. 7, the fact that larger CSR that does not fail the specimen results in more strengthening of the sample may be partly due to a larger change in effective stress (affected by the pore pressure change) and larger increase in density with drainage. Fig. 9 shows that the volumetric strain increase after drainage can be well-correlated with the pore pressure increase by the preceding undrained cyclic loading phase before liquefaction takes place. Here we use eq.(11) with ΔV the volume change during reconsolidation, and V the sample volume during the immediate past undrained cyclic loading phase. Shamoto et al. [38] found similar results with stress-controlled undrained cyclic triaxial tests on Toyoura sand followed by drainage. Fig. 9 also shows that the correlation of volumetric compression and pore pressure change is independent of the number of past seismic events.

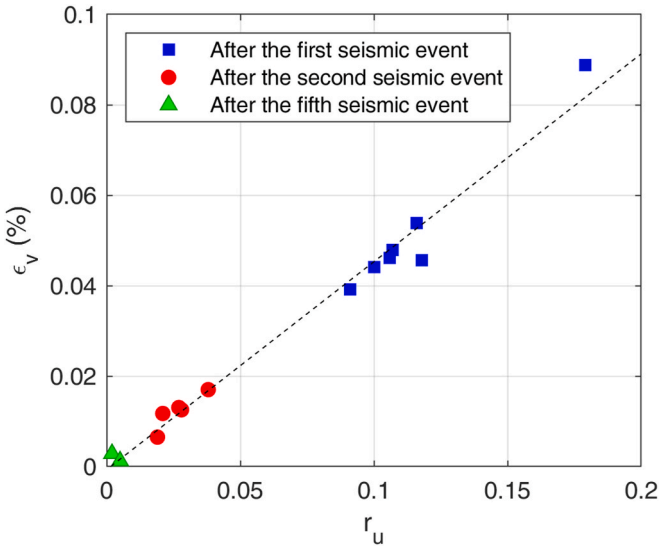

Fig. 9. Relationship between the excess pore pressure ratio generated in the undrained cyclic loading phase, and the volumetric strain due to following reconsolidation.

However, the density increase might not be the most significant factor that governs seismic strengthening. From Table 2 it can be seen that for one seismic event that does not fail the sample, the increase in relative density (change of absolute values of 0.3–0.6%) is less than the error in sample preparation (D_R can be $\pm$ 3% different from the target value 25% after consolidation). However, there is a significant increase in the undrained shear strength (change of 17–34%). Therefore, this increase of shear strength is most likely not solely due to an increase in relative density. Koseki et al. [10] and Wahyudi et al. [9] found similar results, and hypothesize that it is due to the change of the sediment's micro-structure associated with the seismic shaking. Wichtmann et al. [7] also found significant strengthening on triaxial specimens with drained cyclic preloading followed by undrained cyclic loading. They found an increase of the intensity of drained cyclic preloading correlated with an increase in liquefaction resistance, similar to the results of Fig. 7.

Our results demonstrate that the stress/strain history (i.e. prior seismic events that do not fail the sample) may have a profound influence on the static shear strength of sand. Consequently, the shear strength of a material obtained in an earthquake-prone area cannot be described by the in-situ density alone. The strength is significantly influenced by the past earthquake history, and may change in the future due to small to moderate earthquakes that do not fail the soil.

7.2. Change in static shear strength due to multiple seismic events

As shown in Figs. 8b and 9, the pore pressure generated by multiple seismic events tend to decrease, which indicates an increase in liquefaction resistance (i.e. cyclic shear strength). The increase of liquefaction resistance by multiple seismic events without failure has been studied by e.g. Wang et al. [39] with pluviated sand samples, and Dobry et al. [40] with field observations on natural sand. However, as shown in Figs. 7 and 8a, the monotonic undrained shear strength only increases once and tends to decrease after two rounds of seismic events compared with only one round of seismic event. This phenomenon becomes even more interesting as monotonic shear strength does not follow the expected trend as cyclic shear strength. We hypothesize that this may also be caused by a change in the sediment's microstructure (particle re-orientation), which may have a destructive effect that overwhelms

the strengthening effect from the density increase, and only influences the monotonic shear strength but not the cyclic shear strength. In Table 3 and Fig. 8, it was shown that the change of undrained shear strength generally corresponds to the change of Gmax (derived from shear wave velocity). However, despite the expected increase of cyclic shear strength, the shear wave velocity (and the monotonic shear strength) may not necessarily increase accordingly. This observation was also found in El-Sekelly et al. [41] who performed centrifuge tests on silty sand and found that the increase in cyclic strength caused by prior seismic shaking without failure did not result in a corresponding increase in the shear wave velocity (measured by bender elements) of the soil.

7.3. Potential changes in sand structure

Alshibli et al. [42] performed CT scans of a drained triaxial monotonic-loaded Ottawa F-75 sample and found that the arrangement of the sand particles was highly inhomogeneous, with failure of the specimens characterized by circular shear cones and multiple shear bands demonstrating lower densities where the material dilated during shearing. Oda et al. [43] discussed the construction of a highly anisotropic column-like structure and connected voids, which started growing in the "preshearing" process in their triaxial test (in our case, it is the prior seismic shaking without failure). The anisotropy grew parallel to the major principal stress direction and could grow without changing the global void ratio much. The structure became unstable when the major stress was rotated. In our case with a cyclic triaxial test on an isotropically-consolidated specimen, there is a 90° rotation of the major principal stress' direction between the two halves of the loading cycle. From a micro-structural point of view, a destruction of the existing elongated voids might be induced by the second seismic event, when the induced axial strain changes direction (Fig. 8b). To further prove this hypothesis, particle-scale numerical modeling will be needed in the future.

Gutierrez [44] conducted CT analysis on Ottawa 20/30 specimens liquefied after shake table tests, and the results showed that even though the soil was observed to have densified (settled) after liquefaction, some pockets of loose soil (i.e. high void ratio) were observed during image processing. These soil pockets were along the rim of a possible sand boil that went through the middle of the specimen. The occurrence of some strain by cyclic loading, although just small values, also results in a non-cylindrical shape of the specimen which makes the applied deviator stress non-uniform. Teparaksa and Koseki [8] did repeated liquefaction tests in a triaxial apparatus and suggested to limit the tests up to 3–4 stages of liquefaction because of the non-uniform shapes of the specimens after shearing.

In our study, we intentionally impose small seismic shakings with the aim not to liquefy the specimen. However, there may still be some zones of loosened soil in the specimen due to the upward flow of pore water pressure. Fig. 10 shows the patterns of two stages of earthquakes in Test24 (15 cycles of CSR ~ 0.167). Fig. 10 shows that even though the second earthquake has net pore pressure buildup being positive, it generates negative pore pressure when the deviator stress is applied in the extensional domain. This is not observed during the first earthquake event. It suggests that the second earthquake acting on a densified material may induce more dilative behavior during shear, which may have caused the formation of micro-shear bands like those observed by Alshibli et al. [42]. Therefore, local void ratios in the shear bands might deviate from the measured global void ratio. These shear bands may eventually decrease the undrained shear strength of the material even after reconsolidation and global densification. These shear bands may also lower the transmission of shear waves, thus decreasing the shear wave velocity and the calculated shear modulus of the material.

Our observations are similar to Wang et al. [39]; who conducted shake table tests on F50 Ottawa sand with multiple liquefaction stages. They found that the first partial liquefaction stage without failure that induced negative pore pressure (dilatancy) of the specimen (their Event #4-1) temporarily reduced the specimen's liquefaction resistance in the subsequent shaking event, whereas in previous events when the excess pore pressure was positive the liquefaction resistance only increased after reconsolidation. Wang et al. [39] also studied the cone penetration resistance before and after each shaking event and observed that prior seismic events without failure significantly disturbed the existing soil structure and reduced the cone resistance at shallow depths, but increased the cone resistance at deeper depths after reconsolidation. These results show that prior seismic shaking can cause a significant disturbance in the homogeneity of a sample, as the process involves upward migration of the fluid with excess pore pressure. The bottom of the sample might be more efficiently compacted than the top of the sample where particles were suspended during liquefaction. For future analysis, we suggest to perform CT scans during the process of cyclic loading to directly observe the change in the sediments' microstructure.

In addition, if there is particle crushing, grain size reduction plus the change in angularity may also play a role on the shear strength. This effect was estimated by sieve analysis (Appendix E) on Ottawa Sand 20/30 before and after triaxial tests. After being reused about 8 times, the median particle size (D_{50}) was reduced by approximately 0.02 mm, and the percentage of grains finer than 0.63 mm increased from 13% to 22% (Fig. (E.1)). It may further increase the difference of internal structures of two specimens even though the measured global void ratio (thus the relative density) may be similar. Given the low effective stress tested in this study, we assume that it is more likely to be grain abrasion instead of

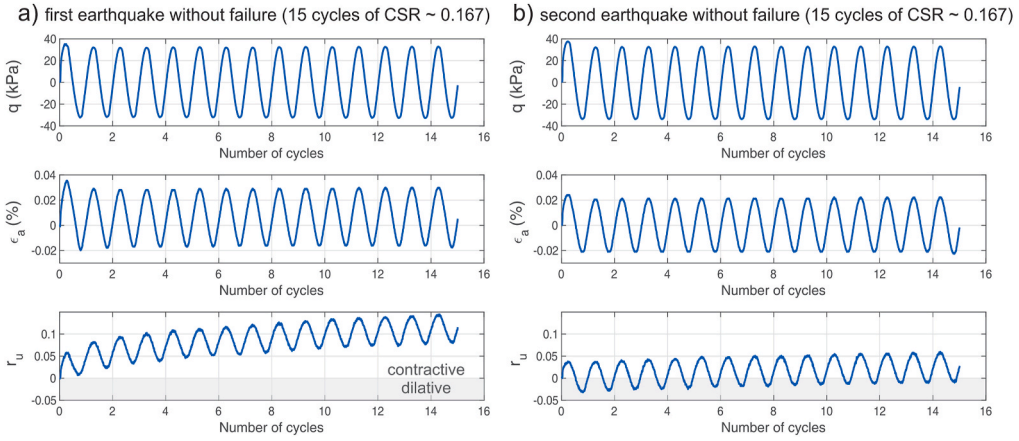

Fig. 10. Comparison of two earthquake stages (15 cycles of CSR ~ 0.167) in Test24. Note that the second earthquake generates negative pore pressure in the extensional domain, whereas the first earthquake only generates positive pore pressure.

crushing. However, we estimate that the impact of grain abrasion to our test results might not be significant because: 1. Despite the finer sand portion increase, still 99% of the sand is coarser than the definition of fine sand (0.42 mm) according to the Unified Soil Classification System (USCS). 2. Testing materials in this study were reused 4 times maximum, so the abrasion impact should be smaller than in Fig. (E.1). 3. In addition, repetition monotonic tests Test9 and Test26 (being reused twice maximum) were in good agreement with each other (Fig. 3). Gmax of all the $D_R \sim 25\%$ specimens in this study do not deviate too much from 97 MPa after consolidation (Table 2). To further investigate the effect of particle size change on the undrained shear strength, more analyses are needed in the future.

7.4. Potential different effect of seismic strengthening between sand and clay

The result in this study that undrained shear strength does not increase after multiple seismic events is contrary to O'Loughlin et al. [45] who used load-controlled cyclic T-bar tests to assess effects of cyclic loading and reconsolidation on kaolin clay. 20 cycles mobilizing 25%–75% initial monotonic strength led to 2.1 and 2.5 times the initial monotonic strength after the first and second consolidation periods. Their result seems to better demonstrate the observations from natural settings in e.g. Moernaut et al. [46] who found that undrained shear strength increased with sediment age in both Chilean lakes and Japan Trench margin, suggesting a cumulative strengthening effect where the sediment had experienced a long earthquake history. Song et al. [11] showed that after wave-induced liquefaction and reconsolidation process, the monotonic shear strength of the Yellow River seabed silt was enhanced, and exhibited an overconsolidation characteristic in comparison to non-liquefied silt.

In the marine deposition environment (usually composed of cohesive silt or clay), the increase of shear strength caused by overconsolidation may have different origins: 1) mechanical origin (e.g. erosion, mechanical loading), and 2) chemical origin (e.g. cementation, bioturbation, ionic exchange, aging) (e.g. Refs. [47,48]). By testing cohesionless sand, we can rule out the chemical origin and expect that the change of strength is caused by mechanical loading and the change of effective stress during cyclic loading and reconsolidation processes (Fig. 6). Our results demonstrate the possible mechanical effect caused by small to moderate seismic shocks, but it may not be significant enough to present the field observation that active margins have 2–3 times larger shear strength than passive margins after multiple events [3]. In addition, O'Loughlin et al. [45] showed that soil with higher sensitivity gains greater strength after reconsolidation. Therefore, clay-related cohesion and sensitivity may play important roles on seismic strengthening in marine settings. For future studies, we suggest to test natural clayey materials and account more realistically for their geologic ages (aging effect + seismic history). To evaluate the earthquake history around a potential submarine landslide site, it requires further geologic investigation such as determining the age of existing landslide deposits.

8. Summary and conclusions

The objective of this paper was to enhance our understanding of the effect of prior seismic shaking on the monotonic undrained shear strength of a granular material and its dependence on parameters such as seismic intensity and the number of seismic events. To achieve this objective we performed a series of triaxial experiments on Ottawa Sand. The specimens were first subjected to undrained cyclic loading followed by reconsolidation allowing drainage. Afterwards, drainage was closed and undrained shear strength was determined by monotonic loading. The experimental data show that without a significant change in the relative density (1%), the monotonic undrained shear strength can be increased by 34% due to small to moderate seismic events. The small-strain shear modulus (mechanical stiffness) obtained by bender element tests also generally increased after reconsolidation of the first seismic event and the strengthening effect increased as the seismic intensity increased. However, the results did not show a clear increase in monotonic undrained shear strength for more than one seismic event. One possible reason for this behavior could be changes in the soil microstructure. However, more research is needed to confirm this hypothesis. Future research could include investigating the effects of particle re-orientation by seismic shaking, variability in local void ratio, examining the effect of increasing the heterogeneity of the specimen, comparing results between triaxial and direct simple shear devices, and performing tests for clayey material with a higher initial void ratio.

The results of this study provide much needed information to assess the change in the static slope stability after small to moderate events have occurred, which is not only relevant to submarine landslide and tsunami risk assessment, but also to other geotechnical practices such as the design and maintenance of platform foundations, submarine pipelines and cables. However, we only tested Ottawa Sand 20/30 with one effective confining stress (100 kPa) and one relative density (25%). More tests are needed with different sediment types such as clays, and sand with more fines, as well as different confining stresses and loading conditions to provide a comprehensive understanding of the effect of seismic strengthening.

Credit Author Statement

Ting-Wei Wu: Conceptualization, Methodology, Software, Formal analysis, Investigation, Data curation, Writing- Original Draft, Visualization. **Yusuke Suzuki:** Methodology, Software, Supervision, Writing - Review & Editing, Visualization. **Brian Carlton**: Methodology, Supervision, Writing - Review & Editing, Visualization. **Carl Harbitz**: Resources, Supervision, Project administration, Funding acquisition. **Achim Kopf**: Conceptualization, Supervision, Project administration, Funding acquisition.

Declaration of competing interest

The authors declare that they have no known competing financial interests or personal relationships that could have appeared to influence the work reported in this paper.

Acknowledgement

This project is funded by the European Union, project SLATE (Submarine landslides and their impact on European continental margins). It has received funding from the Horizon 2020 EU Framework Program for Research and Innovation under the Marie Skłodowska-Curie grant agreement No. 721403. The authors acknowledge the Schmertmann Research Laboratory (SRL) at the Norwegian Geotechnical Institute (NGI) for supporting the triaxial apparatus presented in this work. We thank Amir Kaynia, Maarten Vanneste, and two anonymous reviews for their helpful comments to improve the manuscript. We also thank Morten Sjursen, Helge Rolandsgard and Thomas Vestgården for their technical support and maintenance of the lab facilities. Ting-Wei Wu thanks Nabil Sultan from IFREMER (Center of Brest/Plouzané, France), and her MARUM colleagues Gauvain Wiemer, Dina Al-Sammarraie, Alexander Roesner, and Stefan Kreiter for providing advice with the triaxial testing procedures.

Appendix A. Triaxial Cell

Fig. (A.1) shows the configuration of a triaxial specimen placed in the cell. After filling it fully with water to provide confining pressure, an external compliance calibrator is placed on top of the cell to measure the slight axial deformation of the cell resulting from the change of cell pressure during the test. During the testing process, this small deformation is corrected (subtracted) from the axial deformation measurement of the bottom pedestal. The two cables extending in front of the cell are connected to a separate machine to trigger and receive signals from the bender elements inserted in the specimen.

Appendix B. Bender Elements

Piezoceramic bender elements are incorporated in the triaxial specimen, and a bender element test can be done at any stage during the test. On top of the specimen, the transmitter element generates a sinusoidal pulse with small shear strain (<0.001%) that propagates along the length of the specimen. The receiver element at the bottom of the specimen detects the arrival time of the shear wave. More details are described in Ref. [20]. The shear modulus of the soil at small strains, termed "Gmax", can be calculated using the shear wave velocity V_S calculated from the tip-to-tip distance between the two elements, and the time difference between the major first peaks (as defined in Ref. [49]) of the trigger and the receiver shear waves. Bender element tests are conducted at input frequencies around 12.5 kHz when the effective confining stress is around 100 kPa. Gmax is computed from the formula:

$$G_{max} = Vs^2 \times \rho \tag{B.1}$$

where: Vs = shear wave velocity (m/s) and ρ = density of the soil (kg/m^3). $D_R \sim 25\%$ specimens have Vs about 220 m/s, ρ about 2000 kg/m^3, making Gmax around 97 MPa.

Appendix C. Critical Void Ratio Line

Fig. (C.1) compares the positions of the $D_R \sim 7\%$ and $D_R \sim 25\%$ Ottawa Sand 20/30 samples in this study relative to the critical void ratio line determined by the undrained triaxial testing results from Santamarina and Cho [31].

Appendix D. Young's Modulus and Shear Modulus

Young's modulus (E) during undrained monotonic loading is directly calculated as the ratio of measured axial stress change (equals to the change of deviator stress) to axial strain. Tangent shear modulus (G) is subsequently calculated using the theory of elasticity, assuming Poisson's ratio (ν) equals 0.5 representing fully saturated, undrained conditions.

$$E = \frac{\Delta q}{\Delta \varepsilon_a} \tag{D.1}$$

$$G = \frac{E}{2\,(1+\nu)} \tag{D.2}$$

It can be deduced from eq.(D.2) that the tangent shear modulus is one-third of the Young's modulus. The definition of shear strain (γ) is:

$$\gamma = \varepsilon_a - \varepsilon_r = \varepsilon_a - (-\nu\varepsilon_a) = \varepsilon_a(1+\nu) \tag{D.3}$$

where ε_a is axial strain, ε_r is radial strain, and ν is Poisson's ratio. For an undrained test where $\nu = 0.5$, shear strain is 1.5 times of axial strain. Shear modulus degradation curves with shear strain are plotted in Fig. 3cg.

Appendix E. Grain Abrasion

Particle breakage or abrasion is quantified through a comparison of pre- and post-test particle size distribution curves. Around 80 triaxial tests were conducted between these two measurements, with each test using about 1/10 of the whole available material. Each particle of the sand is therefore estimated to be reused about 8 times between these two grain size measurements. Grain abrasion results in an increase in the number of finer particles, which broadens the grading of particle sizes (dotted blue curves in Fig. (E.1)). Note that the sand used in the experiments in this study (Table 2) was reused only 4 times maximum.

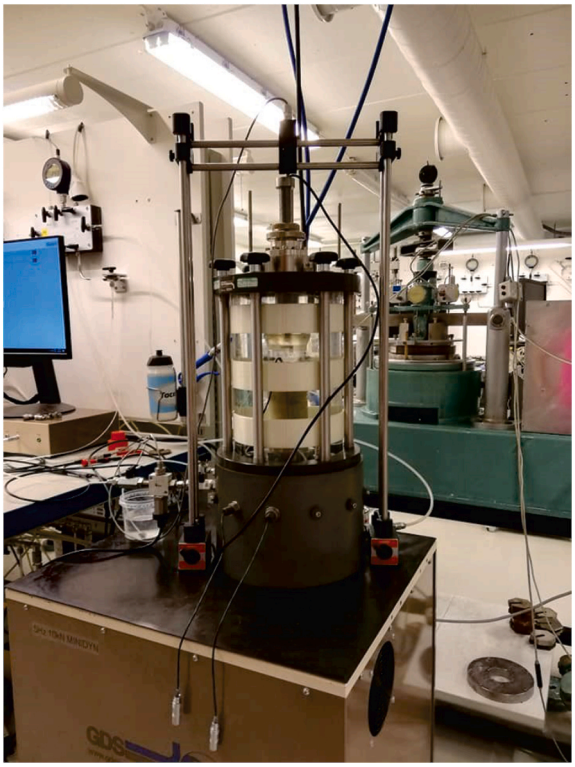

Fig. (A.1). Photo of the triaxial testing system used in this study.

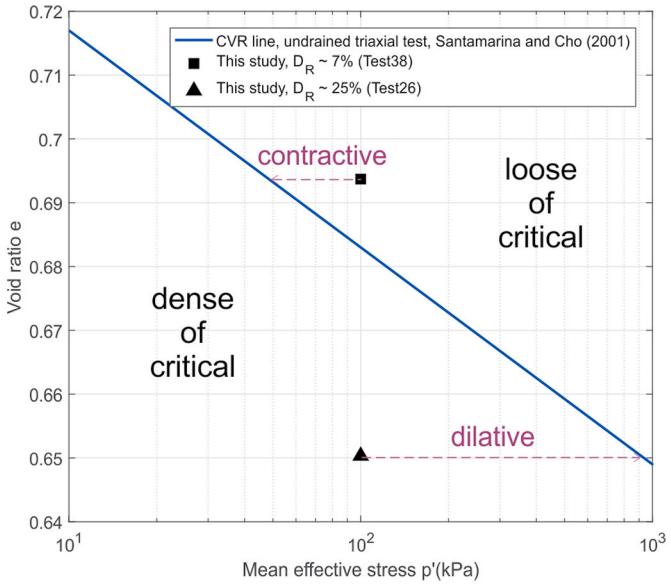

Fig. (C.1). States of the samples used in this study relative to the critical void ratio line (CVR line).

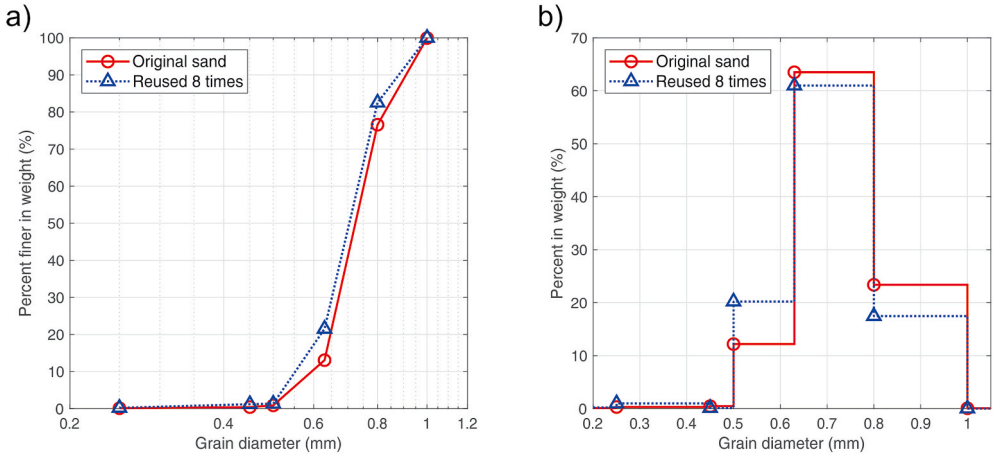

Fig. (E.1). Estimation of grain abrasion of Ottawa Sand 20/30 before and after being reused 8 times. Six sieves are used to do the analysis (0.25, 0.45, 0.5, 0.63, 0.8, 1 mm). (a) Cumulative grain size distribution curves. (b) Mass distribution between each sieve presented in percentage.

References

[1] Shanmugam G. The landslide problem. J Palaeogeogr 2015;4:109–66. https://doi.org/10.3724/SP.J.1261.2015.00071.

[2] Nelson CH, Escutia C, Damuth JE, Twichell JDC. Interplay of mass-transport and turbidite-system deposits in different active tectonic and passive continental margin settings: external and local controlling factors. In: SEPM (society for sedimentary geology); 2011. p. 39–66. https://doi.org/10.2110/sepmsp.096.039.

[3] Sawyer DE, DeVore JR. Elevated shear strength of sediments on active margins: evidence for seismic strengthening. Geophys Res Lett 2015;42:10,216–10,221. https://doi.org/10.1002/2015GL066603.

[4] McAdoo BG, Pratson LF, Orange DL. Submarine landslide geomorphology, US continental slope. Mar Geol 2000;169:103–36. https://doi.org/10.1016/S0025-3227(00)00050-5.

[5] Lee H, Orzech K, Locat J, Boulanger E, Konrad J-M. Seismic strengthening, a conditioning factor influencing submarine landslide development. In: Proceedings of the 57th Canadian geotechnical conference; 2004. p. 8–14.

[6] Strozyk F, Strasser M, Förster A, Kopf A, Huhn K. Slope failure repetition in active margin environments: constraints from submarine landslides in the Hellenic fore arc, eastern Mediterranean. J Geophys Res 2010;115. https://doi.org/10.1029/2009JB006841.

[7] Wichtmann T, Niemunis A, Triantafyllidis T, Poblete M. Correlation of cyclic preloading with the liquefaction resistance. Soil Dynam Earthq Eng 2005;25:923–32. https://doi.org/10.1016/j.soildyn.2005.05.004.

[8] Teparaksa J, Koseki J. Silica sand behavior under repeated liquefaction in cyclic triaxial test. In: Proc. Of 19th international conference on soil mechanics and geotechnical engineering, seoul, korea, september; 2017. p. 17–22.

[9] Wahyudi S, Koseki J, Sato T, Chiaro G. Multiple-liquefaction behavior of sand in cyclic simple stacked-ring shear tests. Int J GeoMech 2015;16:C4015001. https://doi.org/10.1061/(ASCE)GM.1943-5622.0000596.

[10] Koseki J, Aoyagi Y, Morimoto T, Wahyudi S, Teparaksa J, Iqbal MS. Multiple-liquefaction behavior of sands in shaking table tests and cyclic stacked-ring shear tests. In: Presented at the earthquake geotechnical engineering for protection and development of environment and constructions: proceedings of the 7th international conference on earthquake geotechnical engineering (ICEGE 2019), june 17-20 2019, rome Italy; 2019.

[11] Song B, Sun Y, Song Y, Dong L, Du X, Zhou Q, Zhao X. Post-liquefaction re-compaction effect on the cyclic behavior of natural marine silty soil in the Yellow River delta. Ocean Eng 2020;195:106753. https://doi.org/10.1016/j.oceaneng.2019.106753.

[12] Seed HB, Idriss IM. Simplified procedure for evaluating soil liquefaction potential. J Soil Mech Found Div 1971;97:1249–73.

[13] Idriss IM. An update to the seed-idriss simplified procedure for evaluating liquefaction potential. In: Proceedings of TRB workshop on new approaches to liquefaction. Washington DC: Federal Highway Administration; 1999. Publication No. FHWA-RD-99-165.

[14] Youd TL, Idriss IM, Andrus RD, Arango I, Castro G, Christian JT, et al. Liquefaction resistance of soils: summary report from the 1996 NCEER and 1998 NCEER/NSF workshops on evaluation of liquefaction resistance of soils. J Geotech Geoenviron Eng 2001;127:817–33. https://doi.org/10.1061/(ASCE)1090-0241(2001)127:10(817).

[15] Idriss IM, Boulanger RW. Soil liquefaction during earthquakes. Oakland, Calif: Earthquake Engineering Research Institute; 2008, ISBN 978-1-932884-36-4. https://web.archive.org/web/20080705212101/http://www.seisvol.kishou.go.jp/eq/kyoshin/kaisetsu/comp.htm. [Accessed 23 April 2020].

[16] Polito C, Green RA, Dillon E, Sohn C. Effect of load shape on relationship between dissipated energy and residual excess pore pressure generation in cyclic triaxial tests. Can Geotech J 2013;50:1118–28. https://doi.org/10.1139/cgj-2012-0379.

[17] Restek. Certificate of analysis and safety data sheet of Ottawa Sand ASTM 20/30 mesh. catalog number 26137, https://www.restek.com/catalog/view/6606; 2018.

[18] Lunne T, Knudsen S, Blaker Ø, Vestgården T, Powell JJM, Wallace CF, Krogh L, Thomsen NV, Yetginer G, Ghanekar RK. Methods used to determine maximum and minimum dry unit weights of sand: is there a need for a new standard. Can Geotech J 2019;56:536–53. https://doi.org/10.1139/cgj-2017-0738.

[19] Gds. Advanced dynamic triaxial testing system. Retrieved from, https://www.gdsinstruments.com/gds-products/advanced-dynamic-triaxial-testing-system. [Accessed 23 April 2020].

[20] Dyvik R, Madshus C. Lab measurements of Gmax using bender elements. ASCE Ann. Conven., Adv. Art of Testi. Soils Under Cyclic Cond. 1985:186–96.

[21] Ladd RS. Preparing test specimens using undercompaction. GTJ 1978;1:16–23. https://doi.org/10.1520/GTJ10364J.

[22] Skempton AW. The pore-pressure coefficients A and B. Géotechnique. https://doi.org/10.1680/geot.1954.4.4.143; 1954.

[23] ASTM D4767-11. Standard test method for consolidated undrained triaxial compression test for cohesive soils. West Conshohocken, PA: ASTM International; 2011. https://doi.org/10.1520/D4767-11.

[24] Wang S, Luna R. Monotonic behavior of Mississippi river valley silt in triaxial compression. J Geotech Geoenviron Eng 2012;138:516–25. https://doi.org/10.1061/(ASCE)GT.1943-5606.0000603.

[25] Kramer SL. Geotechnical earthquake engineering, Prentice-Hall international series in civil engineering and engineering mechanics. Upper Saddle River, N.J: Prentice Hall; 1996, ISBN 978-0-13-374943-4.

[26] Wang MS. Liquefaction of triaxial sand samples under different frequencies of cyclic loading. London, Canada: University of Western Ontario; 1972. M. S. Dissertation.

[27] Lee K, Vernese FJ. End restraint effects on cyclic triaxial strength of sand. J Geotech Eng Div 1978;104:705–19.

[28] Tatsuoka F, Toki S, Miura S, Kato H, Okamoto M, Yamada S, Yasuda S, Tanizawa F. Some factors affecting cyclic undrained triaxial strength of sand. Soils Found 1986;26:99–116. https://doi.org/10.3208/sandf1972.26.3_99.

[29] Rees SD, Jones CR, Snelling K. Adaptive control implementation for the dynamic cyclic testing of soil specimens. In: Geotechnical engineering for infrastructure and development, conference proceedings. ICE Publishing; 2015. p. 3317–22.

[30] ASTM D5311/D5311M-13. Standard test method for load controlled cyclic triaxial strength of soil. West Conshohocken, PA: ASTM International; 2013. https://doi.org/10.1520/D5311_D5311M-13.

[31] Santamarina JC, Cho GC. Determination of critical state parameters in sandy soils—simple procedure. GTJ 2001;24:185–92. https://doi.org/10.1520/GTJ11338J.

[32] Denekamp SA, Tsur-Lavie Y. The study of relative density in some dune and beach sands. Eng Geol 1981;17:159–73. https://doi.org/10.1016/0013-7952(81)90081-8.

[33] Japan Meteorological Agency. 計測震度の算出方法 (in Japanese). Retrieved from, http://www.data.jma.go.jp/svd/eqev/data/kyoshin/kaisetsu/calc_sindo.htm. [Accessed 23 April 2020].

[34] Central Weather Bureaua, 地震震度與加速度之關係如何? (in Taiwanese Mandarin). https://scweb.cwb.gov.tw/zh-tw/guidance/faqdetail/37. [Accessed 23 April 2020].

[35] Japan Meteorological Agencyb. 震度と加速度 (in Japanese). Retrieved from, https://web.archive.org/web/20080705212101/http://www.seisvol.kishou.go.jp/eq/kyoshin/kaisetsu/comp.htm. [Accessed 23 April 2020].

[36] Central Weather Bureau. 震度新分級 應變更實用 (in Taiwanese Mandarin). Retrieved from, https://www.cwb.gov.tw/Data/service/Newsbb/CH/1081218earthquakepress.pdf. [Accessed 23 April 2020].

[37] Toki S, Kitago S. 乾燥砂の変形特性に及ぼす動的繰返し応力の影響 (effects of repeated loading on deformation behavior of dry sand) (in Japanese). Soils Found 1974;14:95–103. https://doi.org/10.3208/sandf1972.14.95.
[38] Shamoto Y, Sato M, Zhang J. Simplified estimation of earthquake-induced settlements in saturated sand deposits. Soils Found 1996;36:39–50. https://doi.org/10.3208/sandf.36.39.
[39] Wang J, Salam S, Xiao M. Evaluation of the effects of shaking history on liquefaction and cone penetration resistance using shake table tests. Soil Dynam Earthq Eng 2020;131:106025. https://doi.org/10.1016/j.soildyn.2019.106025.
[40] Dobry R, Abdoun T, Stokoe KH, Moss RES, Hatton M, El Ganainy H. Liquefaction potential of recent fills versus natural sands located in high-seismicity regions using shear-wave velocity. J Geotech Geoenviron Eng 2015;141:04014112. https://doi.org/10.1061/(ASCE)GT.1943-5606.0001239.
[41] El-Sekelly W, Dobry R, Abdoun T, Steidl JH. Centrifuge modeling of the effect of preshaking on the liquefaction resistance of silty sand deposits. J Geotech Geoenviron Eng 2016;142:04016012. https://doi.org/10.1061/(ASCE)GT.1943-5606.0001430.
[42] Alshibli KA, Sture S, Costes NC, Frank ML, Lankton MR, Batiste SN, Swanson RA. Assessment of localized deformations in sand using X-ray computed tomography. GTJ 2000;23:274–99. https://doi.org/10.1520/GTJ11051J.
[43] Oda M, Kawamoto K, Suzuki K, Fujimori H, Sato M. Microstructural interpretation on reliquefaction of saturated granular soils under cyclic loading. J Geotech Geoenviron Eng 2001;127:416–23. https://doi.org/10.1061/(ASCE)1090-0241(2001)127:5(416).
[44] Gutierrez A. The impact of liquefaction on the microstructure of cohesionless soils. Tempe, Arizona: MS Thesis, Arizona State University; 2013. https://repository.asu.edu/items/18740.
[45] O'Loughlin CD, Zhou Z, Stanier SA, White DJ. Load-controlled cyclic T-bar tests: a new method to assess effects of cyclic loading and consolidation. Géotech Lett 2020;10:7–15. https://doi.org/10.1680/jgele.19.00030.
[46] Moernaut J, Wiemer G, Wu T-W, Molenaar A, Kopf A, Strasser M. Seismic strengthening of diatom-rich sediments: a comparison of slope sediments from Chilean lakes and the Japan Trench margin. In: Abstracts of European geosciences union (EGU) general assembly, EGU2020-2578, 4-8 may 2020; 2020. https://doi.org/10.5194/egusphere-egu2020-2578. Sharing Geoscience Online.
[47] Sultan N, Cochonat P, Dennielou B, Bourillet J-F, Savoye B, Colliat J-L. Surconsolidation apparente et pression osmotique dans un sédiment marin. Comptes Rendus Acad Sci - Ser IIA Earth Planet Sci 2000;331:379–86. https://doi.org/10.1016/S1251-8050(00)01419-1.
[48] Yenes M, Monterrubio S, Nespereira J, Casas D. Apparent overconsolidation and its implications for submarine landslides. Eng Geol 2020;264:105375. https://doi.org/10.1016/j.enggeo.2019.105375.
[49] Lee J-S, Santamarina JC. Bender elements: performance and signal interpretation. J Geotech Geoenviron Eng 2005;131:1063–70. https://doi.org/10.1061/(ASCE)1090-0241(2005)131:9(1063).
[50] Sandoval EA, Pando MA. Experimental assessment of the liquefaction resistance of calcareous biogenous sands. Earth Sci Res J 2012;16:55–63.